Nanoscale

PAPER

View Article Online
View Journal | View Issue

Cite this: *Nanoscale*, 2016, **8**, 12683

Long circulating reduced graphene oxide–iron oxide nanoparticles for efficient tumor targeting and multimodality imaging

Cheng Xu,[a,b] Sixiang Shi,[c] Liangzhu Feng,[d] Feng Chen,[b] Stephen A. Graves,[e] Emily B. Ehlerding,[e] Shreya Goel,[c] Haiyan Sun,[b] Christopher G. England,[e] Robert J. Nickles,[e] Zhuang Liu,[d] Taihong Wang*[a] and Weibo Cai*†[b,c,e,f]

Received 24th December 2015,
Accepted 1st April 2016

DOI: 10.1039/c5nr09193d

www.rsc.org/nanoscale

Polyethylene glycol (PEG) surface modification is one of the most widely used approaches to improve the solubility of inorganic nanoparticles, prevent their aggregation and prolong their *in vivo* blood circulation half-life. Herein, we developed double-PEGylated biocompatible reduced graphene oxide nanosheets anchored with iron oxide nanoparticles (RGO–IONP–^{1st}PEG–^{2nd}PEG). The nanoconjugates exhibited a prolonged blood circulation half-life (~27.7 h) and remarkable tumor accumulation (>11 %ID g^{-1}) *via* an enhanced permeability and retention (EPR) effect. Due to the strong near-infrared absorbance and superparamagnetism of RGO–IONP–^{1st}PEG–^{2nd}PEG, multimodality imaging combining positron emission tomography (PET) imaging with magnetic resonance imaging (MRI) and photoacoustic (PA) imaging was successfully achieved. The promising results suggest the great potential of these nanoconjugates for multi-dimensional and more accurate tumor diagnosis and therapy in the future.

1. Introduction

Inorganic nanoparticle-based contrast agents with a strong signal output and multifunctionality have shown great potential for efficient tumor diagnosis and therapy.[1,2] However, inorganic nanoparticles are generally insoluble and easy to aggregate in a physiological environment, severely limiting their applications to *in vivo* tumor targeting.[3,4] To overcome this limitation, conjugating biocompatible polymers (*e.g.* polyethylene glycol (PEG)) onto nanoparticles is one of the most commonly used methods.[5–7] The PEG chains can effectively improve the solubility and prevent aggregation of nanoparticles by passivating their surface and diminishing their association with serum and opsonin.[8–10] Of note, as reported in our previous work, enhanced stability of nanoparticles was achieved by decorating two types of PEG chains in comparison with a single type or non-PEGylated nanoparticles.[11] Furthermore, optimizing the PEGylation of nanoparticles can also prolong their circulation time in blood and reduce the uptake by the reticuloendothelial system (RES), in which NPs are rapidly shuttled out of circulation to the liver, spleen or bone marrow.[3,12] Numerous studies have reported that a denser PEG coating and larger PEG chains will result in a longer circulation time *in vivo*,[13] which allows nanoparticles to continuously pass through the tumor vasculature and passively accumulate in tumor sites at a higher concentration than the healthy tissue due to an enhanced permeability and retention (EPR) effect.[14–16]

Reduced graphene oxide (RGO) nanosheets with high near-infrared (NIR) light absorbance and biocompatibility have recently been applied in hyperthermia tumor therapy,[17–19] drug delivery[20–22] and bioimaging.[23,24] Our previous studies have demonstrated that the antibody conjugated radiolabeled RGO conjugate can specifically target the tumor vasculature and be promptly detected by positron emission tomography (PET) imaging.[25] With high sensitivity and by providing a clear visualization of the solid tumor and quantitative information, PET imaging is an excellent technique for diagnosing and

---

[a] *Key Laboratory for Micro-Nano Optoelectronic Devices of Ministry of Education and State Key Laboratory for Chemo/Biosensing and Chemometrics, Collage of Biology, Hunan University, Changsha, 410082, People's Republic of China. E-mail: thwang@aphy.iphy.ac.cn*

[b] *Department of Radiology, University of Wisconsin–Madison, WI 53792, USA. E-mail: wcai@uwhealth.org*

[c] *Materials Science Program, University of Wisconsin–Madison, WI 53706, USA*

[d] *Institute of Functional Nano & Soft Materials (FUNSOM), Collaborative Innovation Center of Suzhou Nano Science and Technology, the Jiangsu Key Laboratory for Carbon-Based Functional Materials & Devices, Soochow University, Suzhou, Jiangsu 215123, People's Republic of China*

[e] *Department of Medical Physics, University of Wisconsin–Madison, WI 53705, USA*

[f] *University of Wisconsin Carbone Cancer Center, Madison, WI 53705, USA*

† Present Addresses: Departments of Radiology and Medical Physics, University of Wisconsin – Madison, Room 7137, 1111 Highland Avenue, Madison, WI 53705-2275, USA.

determining the stages of many types of tumors.[26] However, PET imaging fails to convey anatomical information and detect early lesions due to its limited spatial resolution.[27] In contrast, magnetic resonance imaging (MRI) offers excellent soft-tissue contrast with a higher resolution.[28] In addition, RGO-based nanomaterials exhibited high NIR absorbance, which can be employed as a strong photoacoustic (PA) imaging contrast agent with a high spatial resolution (up to 50–500 μm) and deep tissue penetration (up to 5 cm).[29,30] By combining PET imaging with MRI and PA imaging as an integrated imaging system, high-order multimodality imaging (PET/MRI/PA) can overcome the limitations of each modality independently and result in obtaining a higher quality and more useful data.[31] More importantly, since PA imaging and MRI display the real biodistribution of nanoparticles in a tumor site rather than the distribution of the isotopes, multimodality imaging (PET/MRI/PA) can better render the *in vivo* fate of nanoparticles and provide more accurate diagnosis and prognosis in future applications.[32–36]

In this work, we developed a novel multifunctional nanocomposite by decorating reduced graphene oxide nanosheets with iron oxide magnetic nanoparticles (RGO–IONP) and coating two types of PEG chains to achieve a long-circulating multimodality imaging probe. Upon optimal surface modification, the *in vivo* blood circulation half-life and passive tumor targeting efficacy were highly improved. Three different imaging modalities (PET/MR/PA) were subsequently conducted, which revealed multi-aspects and more precise information of tumors.

2. Experimental

2.1 Reagents and materials

All reagents were of analytical or higher grade. *S*-2-(4-Isothiocyanatobenzyl)-1,4,7-triazacyclononane-1,4,7-triacetic acid (*p*-SCN-Bn-NOTA) was purchased from Macrocyclics, Inc. (Dallas, TX). Succinimidyl carboxymethyl PEG maleimide (SCM-PEG-Mal; molecular weight: 5 kDa) was purchased from Creative PEGworks (Winston Salem, NC). Chelex 100 resin (50–100 mesh) was purchased from Sigma Aldrich (St Louis, MO). Water and all buffers were of Millipore grade and pretreated with Chelex 100 resin to ensure that the aqueous solution was free of heavy metal. All other reaction chemicals and buffers were obtained from Thermo Fisher Scientific (Fair Lawn, NJ).

2.2 Characterization

Transmission electron microscopy (TEM) images were obtained by using a Tecnai TF-30, 300 kV field emission TEM. Size analysis was performed on a Nano-ZS90 Zetasizer (Malvern Instruments Ltd). The Fourier transform infrared (FT-IR) spectrum was recorded by an Equinox 55/S FT-IR/NIR spectrophotometer. The iron concentration in solution was measured by Microwave Plasma-Atomic Emission Spectroscopy (MP-AES).

2.3 Syntheses of NOTA–RGO–IONP–^{1st}PEG and NOTA–RGO–IONP–^{1st}PEG–^{2nd}PEG nanocomposites

RGO–IONP nanoparticles were prepared from graphene oxide and iron chloride hexahydrate *via* a hydrothermal reaction according to our previous protocol.[30,37] In brief, GO was produced by a modified Hammers method. 0.1 g GO was then dissolved in 20 ml ethylene glycol/diethylene glycol solution (ethylene glycol : diethylene glycol = 1 : 19, by volume). 1.5 g of sodium acrylate, 1.5 g of sodium acetate and 0.54 g of $FeCl_3 \cdot 6H_2O$ were added into GO solution and then transferred to a Teflon-lined stainless-steel autoclave and sealed before heating at 200 °C for 10 h. The resulting RGO–IONP was washed by ethanol and water several times.

The first PEG, C_{18}PMH-PEG$_{5000}$-NH$_2$ (poly (maleic anhydride-*alt*-1-octadecene)-PEG$_{5000}$-NH$_2$), was modified on RGO–IONP by hydrophobic interactions between the C_{18}PMH chain and RGO as reported by our previous study.[9,38] The obtained RGO–IONP–^{1st}PEG was purified by centrifugation with 300 kDa MWCO filters at 4500 rpm for 6 min (repeated 7 times) to further remove free PEG. Then *p*-SCN-Bn-NOTA was added to RGO–IONP–^{1st}PEG in a molar ratio of 10 : 1 at pH 9.0 for 24 h, where the chemical reaction happened between SCN groups and NH$_2$ groups. The resulting NOTA–RGO–IONP–^{1st}PEG was purified by size exclusion column chromatography 10K using PBS as the mobile phase. Most NH$_2$ groups were still present on the surface of NOTA–RGO–IONP–^{1st}PEG for further functionalization. Subsequently, NOTA–RGO–IONP–^{1st}PEG was reacted with SCM-PEG$_{5000}$-Mal ^{2nd}PEG at a molar ratio of 1 : 200 at pH 8.5 for 2 h to form a stable amide bond, based on the reaction between the amino group at the end of the ^{1st}PEG and NHS ester at the end of the ^{2nd}PEG. The resulting NOTA–RGO–IONP–^{1st}PEG–^{2nd}PEG was purified by centrifugation with 100 kDa MWCO Amicon filters at 9500 rpm for 10 min (repeated 5 times).

2.4 Cell lines and animal model

4T1 murine breast cancer was obtained from the American Type Culture Collection (ATCC, Manassas, VA) and cultured as previously described.[25] Cells were used for *in vivo* experiments when they reached ~80% confluence. All animal studies were conducted under a protocol approved by the University of Wisconsin Institutional Animal Care and Use Committee. Four or five week old female BALB/c mice (Harlan, Indianapolis, IN) were injected with 2 × 10^6 4T1 cells in the shoulder (for PET and PA imaging) or flank (for MR imaging) to generate the 4T1 breast cancer model. The BALB/c mice were used for *in vivo* experiments when the tumor diameter reached 6–8 mm.

2.5 ^{64}Cu-labeling, *in vivo* blood circulation test and serum stability

^{64}Cu was produced with an onsite cyclotron (GE PETtrace). ^{64}CuCl$_2$ (74 MBq) was diluted in 0.3 mL of 0.1 M sodium acetate buffer (pH 5.0) and mixed with 0.2 mg of NOTA–RGO–IONP–^{1st}PEG or NOTA–RGO–IONP–^{1st}PEG–^{2nd}PEG. The reaction was conducted at 37 °C for 30 min with constant shaking, then

5 μL 0.1 M EDTA (ethylenediaminetetraacetic acid) was added into the solution and shaken another 5 min to remove non-specific bound ^{64}Cu. The resulting ^{64}Cu-NOTA–RGO–IONP–^{1st}PEG or ^{64}Cu-NOTA–RGO–IONP–^{1st}PEG–^{2nd}PEG was purified by PD-10 size exclusion column chromatography using PBS as the mobile phase. The radioactive fractions were collected for further *in vitro* and *in vivo* studies. Blood circulation tests were carried out on ICR mice. Mouse blood (40–50 μL) was directly collected from the orbital sinus at different time points and measured by a gamma counter immediately.

Serum stability studies were carried out to ensure that ^{64}Cu-NOTA–RGO–IONP–^{1st}PEG or ^{64}Cu-RGO–IONP–^{1st}PEG–^{2nd}PEG was sufficiently stable for *in vivo* applications. ^{64}Cu-NOTA–RGO–IONP–^{1st}PEG or ^{64}Cu-NOTA–RGO–IONP–^{1st}PEG–^{2nd}PEG was incubated in 50% mouse serum at 37 °C for up to 48 h. Portions of the mixture were sampled at different time points and filtered through 300 kDa MWCO filters. The radioactivity within the filtrate was measured, and the percentages of the retained (*i.e.*, intact) ^{64}Cu on the ^{64}Cu-NOTA–RGO–IONP–^{1st}PEG or ^{64}Cu-NOTA–RGO–IONP–^{1st}PEG–^{2nd}PEG conjugates were calculated using the equation:

$$\begin{aligned}&{}^{64}\text{Cu}\%\text{ on NOTA-RGO-IONP}\\&=(\text{total radioactivity}-\text{radioactivity in filtrate})/\text{total radioactivity}\\&\times 100\%.\end{aligned}$$

2.6 PET imaging and biodistribution study

PET scans of 4T1 tumor-bearing mice (6 mice per group), at various time points post-injection of 5–8 MBq of ^{64}Cu-NOTA–RGO–IONP–^{1st}PEG or ^{64}Cu-NOTA–RGO–IONP–^{1st}PEG–^{2nd}PEG *via* the tail vein, were performed using a microPET/microCT Inveon rodent model scanner (Siemens Medical Solutions USA, Inc.). Detailed procedures for data acquisition, image reconstruction, and region-of-interest (ROI) analysis of the PET data have been reported previously.[23,25] Quantitative PET data of the 4T1 tumor and major organs were presented as percentage injected dose per gram of tissue (%ID g^{-1}).

To validate that the ROI values based on PET imaging accurately reflected the radioactivity distribution in tumor-bearing mice, *ex vivo* biodistribution studies were conducted at 48 h post-injection (p.i.). After euthanizing the mice, blood, 4T1 tumor, and major organs/tissues were collected and wet-weighed. The radioactivity in the tissue or blood was measured using a gamma counter (PerkinElmer) and presented as %ID g^{-1} (mean ± SD).

2.7 MRI and PA imaging

In vivo T_2-mapped MR imaging was performed at 3 h and 24 h post-injection after intravenous injection of 400 μL NOTA–RGO–IONP–^{1st}PEG–^{2nd}PEG with a Fe concentration of 5.2 mM using a 4.7 T small animal scanner (Agilent Technologies, Santa Clara, CA). Here are the parameters for T_2-mapped MR imaging: Spin Echo Multi-Slice sequence, TR = 1000 ms, TE = 13.8, 18.8, 23.8, 28.8, 33.8, 38.8, 43.8, 48.8, 53.8 and 58.8 ms, averages = 1, dummy scans = 4, matrix size = 128 × 128. The transverse relaxivity (r_2) of NOTA–RGO–IONP–^{1st}PEG–^{2nd}PEG was measured to be 76.1 mM^{-1} s^{-1}. PA imaging was performed on a Vevo LAZR Photoacoustic Imaging System (VisualSonics,

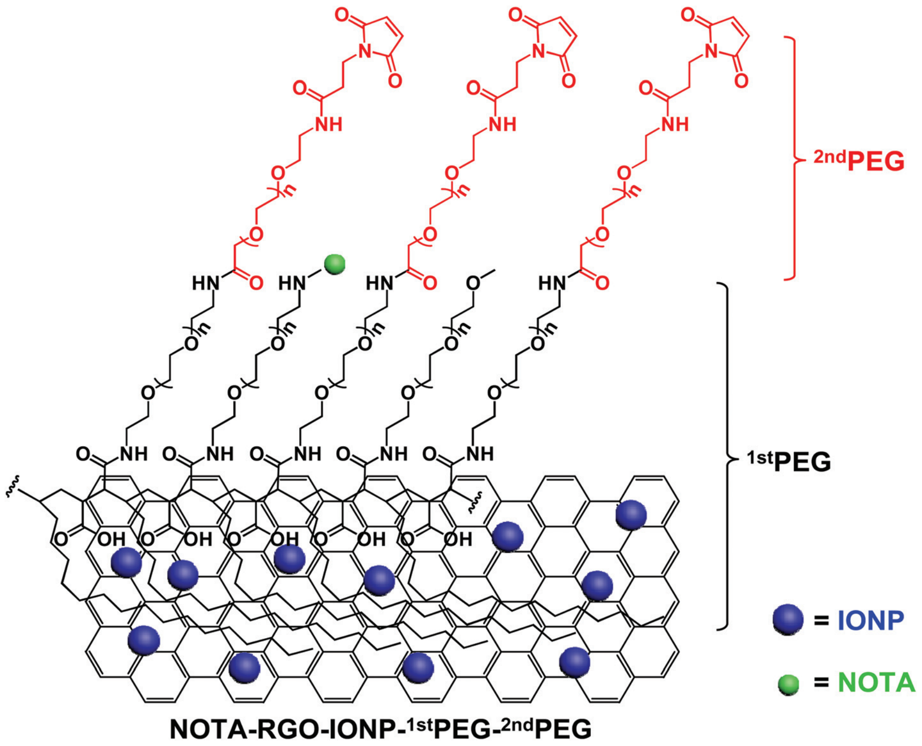

Fig. 1 Schematic illustration of the structure of the NOTA–RGO–IONP–^{1st}PEG–^{2nd}PEG nanocomposite.

Inc., Toronto, Canada) with a laser excitation wavelength of 808 nm and a focal depth of 100 mm. 4T1 tumor-bearing mice were intravenously injected with NOTA–RGO–IONP–^{1st}PEG–^{2nd}PEG (150 μL, 0.3 mg ml^{-1}) and scanned at 24 h post-injection. The same volumes of PBS were injected in 4T1 tumor-bearing mice as control groups.

3. Results and discussion

3.1 Synthesis and characterization

The schematic structure of the NOTA–RGO–IONP–^{1st}PEG–^{2nd}PEG nanocomposite is shown in Fig. 1. Through hydrophobic interaction between the C$_{18}$PMH chain and RGO, ^{1st}PEG was stably attached on the surface of RGO–IONP, which effectively prevented the possible aggregation and provided amino groups for further surface modification. NOTA and ^{2nd}PEG (Mal-PEG$_{5k}$-SCM) were then covalently reacted with the amino groups for chelating radioisotopes and enhancing the blood circulation half-life, respectively. The morphology and structure of RGO–IONP, NOTA–RGO–IONP–^{1st}PEG and NOTA–RGO–IONP–^{1st}PEG–^{2nd}PEG were elucidated by transmission electron microscopy (TEM) measurement, as shown in Fig. 2a–f. Iron oxide nanoparticles (6–8 nm) were evenly distributed on the surface of RGO nanosheets (15–20 nm; Fig. 2a and d). After surface modification with ^{1st}PEG and ^{2nd}PEG, the

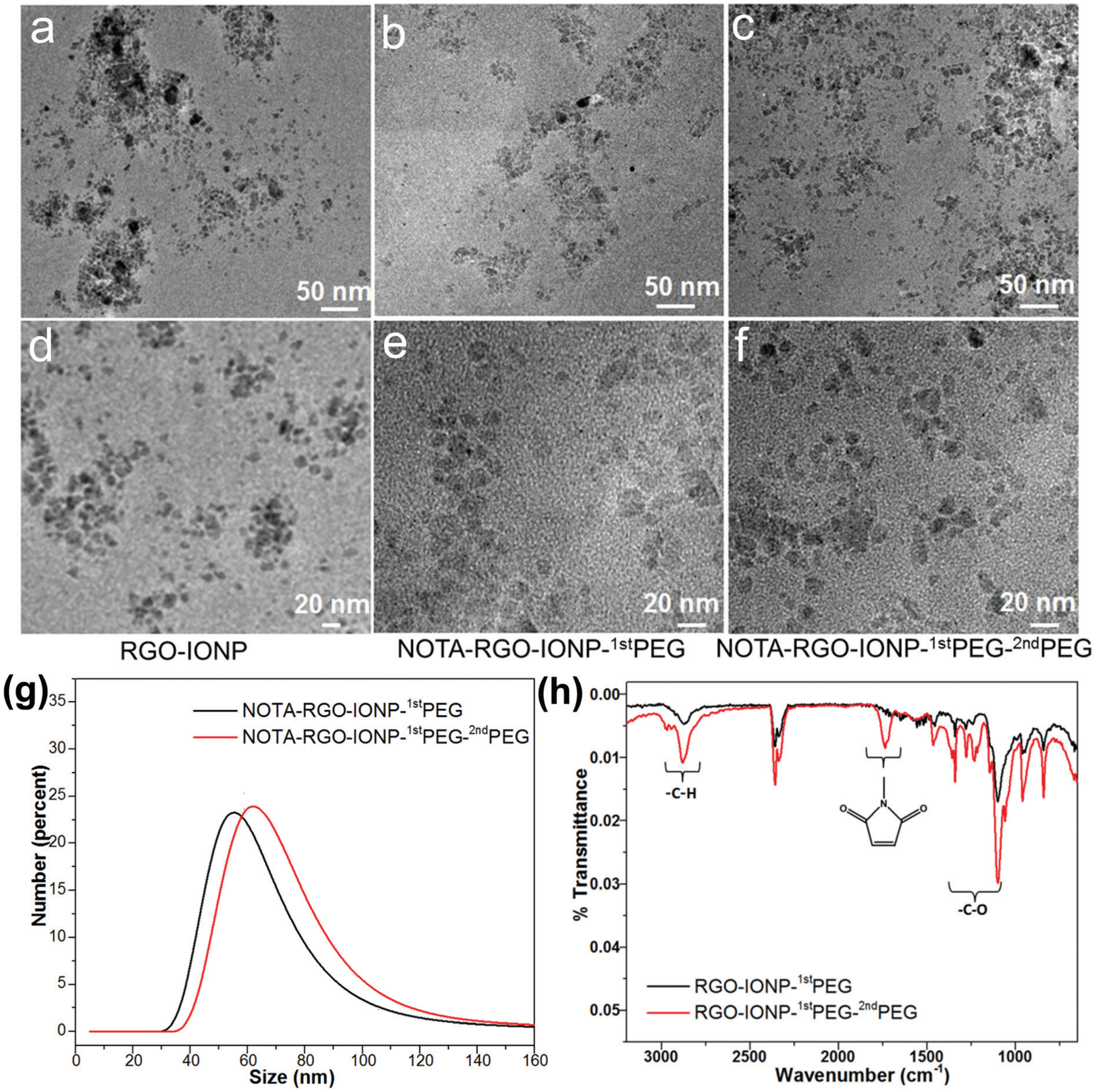

Fig. 2 TEM images of RGO–IONP (a and d), NOTA–RGO–IONP–^{1st}PEG (b and e) and NOTA–RGO–IONP–^{1st}PEG–^{2nd}PEG (c and f). (g) Size analysis of NOTA–RGO–IONP–^{1st}PEG (black line) and NOTA–RGO–IONP–^{1st}PEG–^{2nd}PEG (red line) by DLS. (h) The FT-IR spectrum of RGO–IONP–^{1st}PEG (black line) and RGO–IONP–^{1st}PEG–^{2nd}PEG (red line).

morphologies of NOTA–RGO–IONP–^{1st}PEG and NOTA–RGO–IONP–^{1st}PEG–^{2nd}PEG were almost unchanged (Fig. 2c and f). The hydrodynamic sizes of the NOTA–RGO–IONP–^{1st}PEG and NOTA–RGO–IONP–^{1st}PEG–^{2nd}PEG nanocomposites were then investigated by dynamic light scattering (DLS). As shown in Fig. 2g, the average size of NOTA–RGO–IONP–^{1st}PEG was about 63.8 ± 4.5 nm in PBS solution, while the average size increased to 71.6 ± 3.8 nm after conjugating with ^{2nd}PEG. The sizes measured by DLS were much larger than those by TEM, because TEM solely displayed the morphology of RGO–IONP cores without showing PEG coating.

The presence of functional groups on RGO–IONP–^{1st}PEG and RGO–IONP–^{1st}PEG–^{2nd}PEG nanocomposites was studied by Fourier transform infrared (FT-IR) spectroscopy (Fig. 2h), in which the C–H stretch (~2800 cm^{-1}) and C–O stretch (1100–1500 cm^{-1}) peaks were much stronger on RGO–IONP–^{1st}PEG–^{2nd}PEG than those on RGO–IONP–^{1st}PEG at the same concentration. In addition, the observed peaks of maleimide groups (1700 cm^{-1})[39] on RGO–IONP–^{1st}PEG–^{2nd}PEG clearly demonstrated the successful conjugation of ^{2nd}PEG to RGO–IONP–^{1st}PEG, since the maleimide groups were only present on ^{2nd}PEG.

3.2 *In vivo* blood circulation half-life and serum stability

The *in vivo* blood circulation time of nanoprobes or nanoplatforms is highly correlated with the targeting efficiency in a leaky tumor model,[16] since the extravasation of nanoparticles from the tumor vasculature to an extracellular microenvironment is an accumulative process. Higher nanoparticle concentrations in blood and longer blood elimination half-lives are favorable to improve the tumor targeting efficiency through an enhanced EPR effect.[40] Conjugating another PEG chain on the surface of RGO–IONP–^{1st}PEG could further reduce the contact with proteins and small molecules in blood and improve the circulation time, therefore providing sufficient time for RGO–IONP–^{1st}PEG–^{2st}PEG to not only reach the tumor site but also remain at a high concentration for *in vivo* signal acquisition.

The pharmacokinetics of ^{64}Cu-NOTA–RGO–IONP–^{1st}PEG and ^{64}Cu-NOTA–RGO–IONP–^{1st}PEG–^{2nd}PEG was observed as

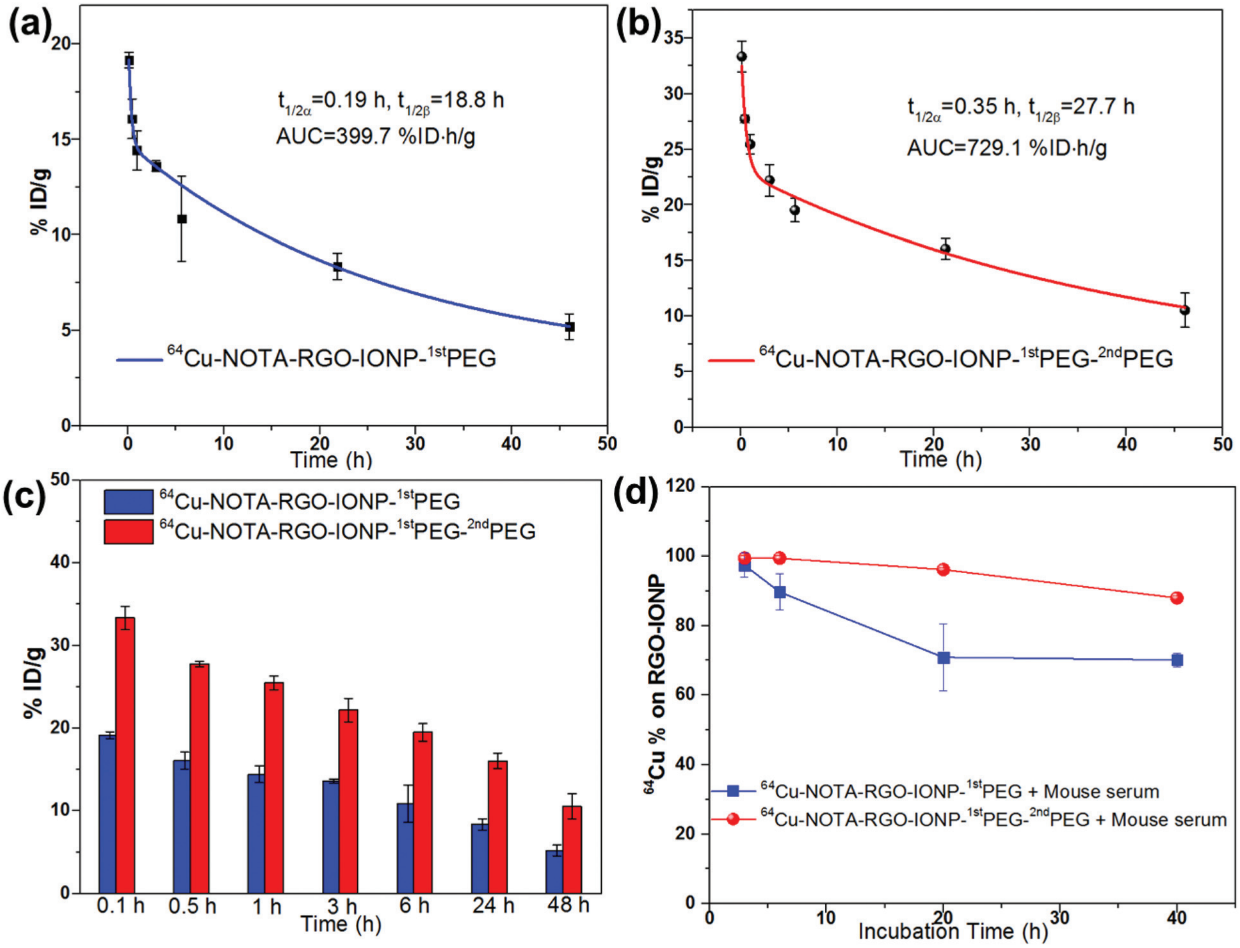

Fig. 3 Blood circulation tests of ^{64}Cu-NOTA–RGO–IONP–^{1st}PEG (a) and ^{64}Cu-NOTA–RGO–IONP–^{1st}PEG–^{2nd}PEG (b), fitting by a two-compartment model with distribution half-life ($t_{1/2\alpha}$) and elimination half-life ($t_{1/2\beta}$). AUC = areas under curve. (c) Histogram of the blood concentration of ^{64}Cu-NOTA–RGO–IONP–^{1st}PEG (blue) and ^{64}Cu-NOTA–RGO–IONP–^{1st}PEG–^{2nd}PEG (red) at different time points from (a) and (b). (d) Serum stability studies of ^{64}Cu-NOTA–RGO–IONP–^{1st}PEG (blue) and ^{64}Cu-RGO–IONP–^{1st}PEG–^{2nd}PEG (red). All data represent 3 mice/times per group.

a two-compartment model with a distribution half-life ($t_{1/2\alpha}$) and elimination half-life ($t_{1/2\beta}$) after intravenous injection (Fig. 3a and b), where the short distribution half-life ($t_{1/2\alpha}$) represents rapid access to each tissue including the tumor region immediately after intravenous injection of the nanoparticles, and the long elimination half-life ($t_{1/2\beta}$) accounts for slow clearance of the nanoparticles from the blood circulation.[13] During the period 0–48 h post-injection, $t_{1/2\alpha}$ of 0.19 h and $t_{1/2\beta}$ of 18.8 h were calculated in ^{64}Cu-NOTA–RGO–IONP coated with only one type of PEG (Fig. 3a), which were basically consistent with our previous study.[30] However, after conjugating with ^{2nd}PEG, the distribution half-life and elimination half-life were remarkably increased to 0.35 h and 27.7 h, respectively (Fig. 3b). The uptake of ^{64}Cu-NOTA–RGO–IONP–^{1st}PEG in blood was 5.2% at 48 h p.i., while the uptake of ^{64}Cu-NOTA–RGO–IONP–^{1st}PEG–^{2nd}PEG was 10.5% at the same time point (Fig. 3c). The overall area under the curve (AUC) of ^{64}Cu-NOTA–RGO–IONP–^{1st}PEG–^{2nd}PEG was 1.8-fold larger than that of ^{64}Cu-NOTA–RGO–IONP–^{1st}PEG, indicating a significant enhancement in the blood circulation half-life after simultaneously coating two types of PEG.

Serum stability studies of ^{64}Cu-NOTA–RGO–IONP–^{1st}PEG and ^{64}Cu-NOTA–RGO–IONP–^{1st}PEG–^{2nd}PEG were subsequently conducted to validate the stability of ^{64}Cu labeling *in vitro* and the feasibility for *in vivo* applications (Fig. 3d). After incubating with mouse serum at 37 °C for 40 h, nearly 90% ^{64}Cu still remained intact on NOTA–RGO–IONP–^{1st}PEG–^{2nd}PEG. In contrast, ^{64}Cu-NOTA–RGO–IONP–^{1st}PEG was not stable and lost 30% ^{64}Cu in the first 20 hours. Similar results were observed from our previous studies as well.[34] The difference in the serum stability between ^{64}Cu-NOTA–RGO–IONP–^{1st}PEG–^{2nd}PEG and ^{64}Cu-NOTA–RGO–IONP–^{1st}PEG was believed to be due to the protecting function of ^{2nd}PEG. With only one time PEGylation, NOTA and ^{64}Cu that were exposed on the surface of nanoparticles directly interacted with the serum proteins, resulting in detachment and excretion through urinary and bile-to-feces pathways in a very short time. The possible detachment of NOTA and ^{64}Cu was significantly reduced after coating ^{2nd}PEG. It also explained why the blood concentrations of ^{64}Cu-NOTA–RGO–IONP–^{1st}PEG–^{2nd}PEG were higher than that of ^{64}Cu-NOTA–RGO–IONP–^{1st}PEG at all the tested time points. Since PET imaging detected isotopes rather than nanoparticles *per se*, high radio-stability in serum made ^{64}Cu-NOTA–RGO–IONP–^{1st}PEG–^{2nd}PEG more preferable for *in vivo* imaging and truly reflects the distribution of nanoparticles.

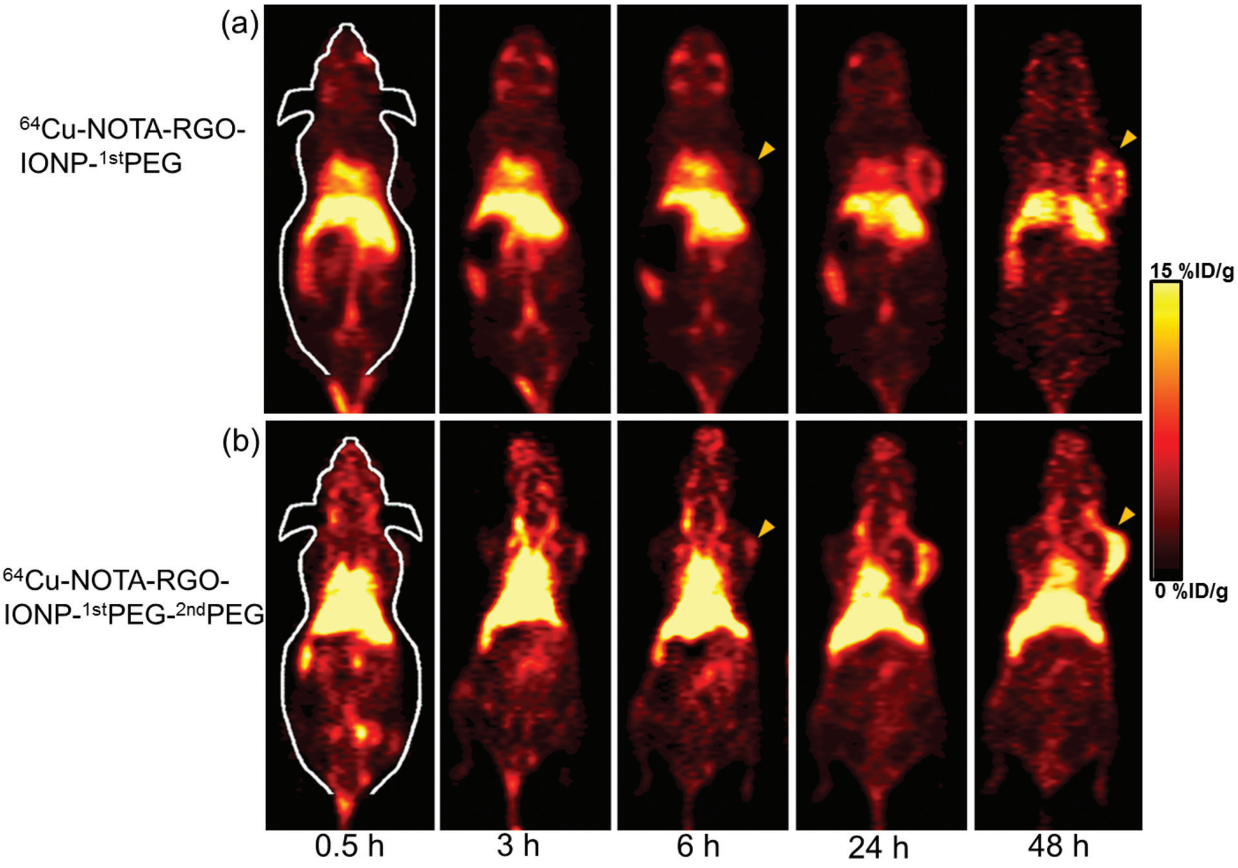

Fig. 4 Serial coronal PET images of 4T1 tumor-bearing mice at different time points post-injection of ^{64}Cu-NOTA–RGO–IONP–^{1st}PEG (a) and ^{64}Cu-NOTA–RGO–IONP–^{1st}PEG–^{2nd}PEG (b). Tumors were indicated by yellow arrowheads.

3.3 PET imaging and biodistribution studies

In consideration of the enhanced blood circulation half-life of ^{64}Cu-NOTA–RGO–IONP–^{1st}PEG–^{2nd}PEG, time points of 0.5 h, 3 h, 6 h, 24 h and 48 h p.i. were chosen for serial PET scans in 4T1 tumor-bearing mice. The PET images post-injection of ^{64}Cu-NOTA–RGO–IONP–^{1st}PEG and ^{64}Cu-NOTA–RGO–IONP–^{1st}PEG–^{2nd}PEG at different time points are shown in Fig. 4a and b respectively. Quantitative data which were obtained from region-of-interest (ROI) analysis of PET data are shown in Fig. 5a and b.

Since the hydrodynamic diameters of ^{64}Cu-NOTA–RGO–IONP–^{1st}PEG and ^{64}Cu-NOTA–RGO–IONP–^{1st}PEG–^{2nd}PEG were above the cutoff for renal filtration (~5 nm), the main clearance was through the hepatobiliary pathway. The liver uptake of ^{64}Cu-NOTA–RGO–IONP–^{1st}PEG–^{2nd}PEG was 32.7 ± 2.5, 33.4 ± 3.7, 33.2 ± 3.4, 30.8 ± 4.4, and 29.5 ± 5.1 %ID g^{-1} at 0.5 h, 3 h, 6 h, 24 h, and 48 h p.i. respectively, while the liver uptake of ^{64}Cu-NOTA–RGO–IONP–^{1st}PEG was lower (20.2 ± 4.2, 19.8 ± 3.7, 19.7 ± 4.6, 17.9 ± 3.9, and 17.4 ± 4.2 %ID g^{-1} at 0.5 h, 3 h, 6 h, 24 h, and 48 h p.i. respectively), possibly due to the lower radio-stability. Both nanocomposites slowly accumulated in the tumor and were clearly visible at 24 h (Fig. 4a and b). However, the tumor uptake of ^{64}Cu-NOTA–RGO–IONP–^{1st}PEG–^{2nd}PEG (2.8 ± 0.5, 4.3 ± 0.8, 5.3 ± 1.2, 12.0 ± 2.0, and 15.5 ± 1.2 %ID g^{-1} at 0.5 h, 3 h, 6 h, 24 h, and 48 h p.i. respectively) was significantly higher than that of ^{64}Cu-NOTA–RGO–IONP–^{1st}PEG (1.6 ± 0.7, 2.4 ± 0.9, 3.3 ± 1.0, 7.2 ± 1.7, and 8.8 ± 2.0 %ID g^{-1} at 0.5 h, 3 h, 6 h, 24 h, and 48 h p.i. respectively), suggesting that ^{64}Cu-NOTA–RGO–IONP–^{1st}PEG–^{2nd}PEG was a better probe for *in vivo* PET imaging. Importantly, 15.5 %ID g^{-1} was one of the highest tumor uptakes that we can achieve based on EPR effects among all the studies using inorganic nanoparticles. In addition, a strong uptake of ^{64}Cu-NOTA–RGO–IONP–^{1st}PEG–^{2nd}PEG was also observed in the heart from 6 h to 48 h and there is almost no uptake in other organs, which was basically consistent with blood circulation

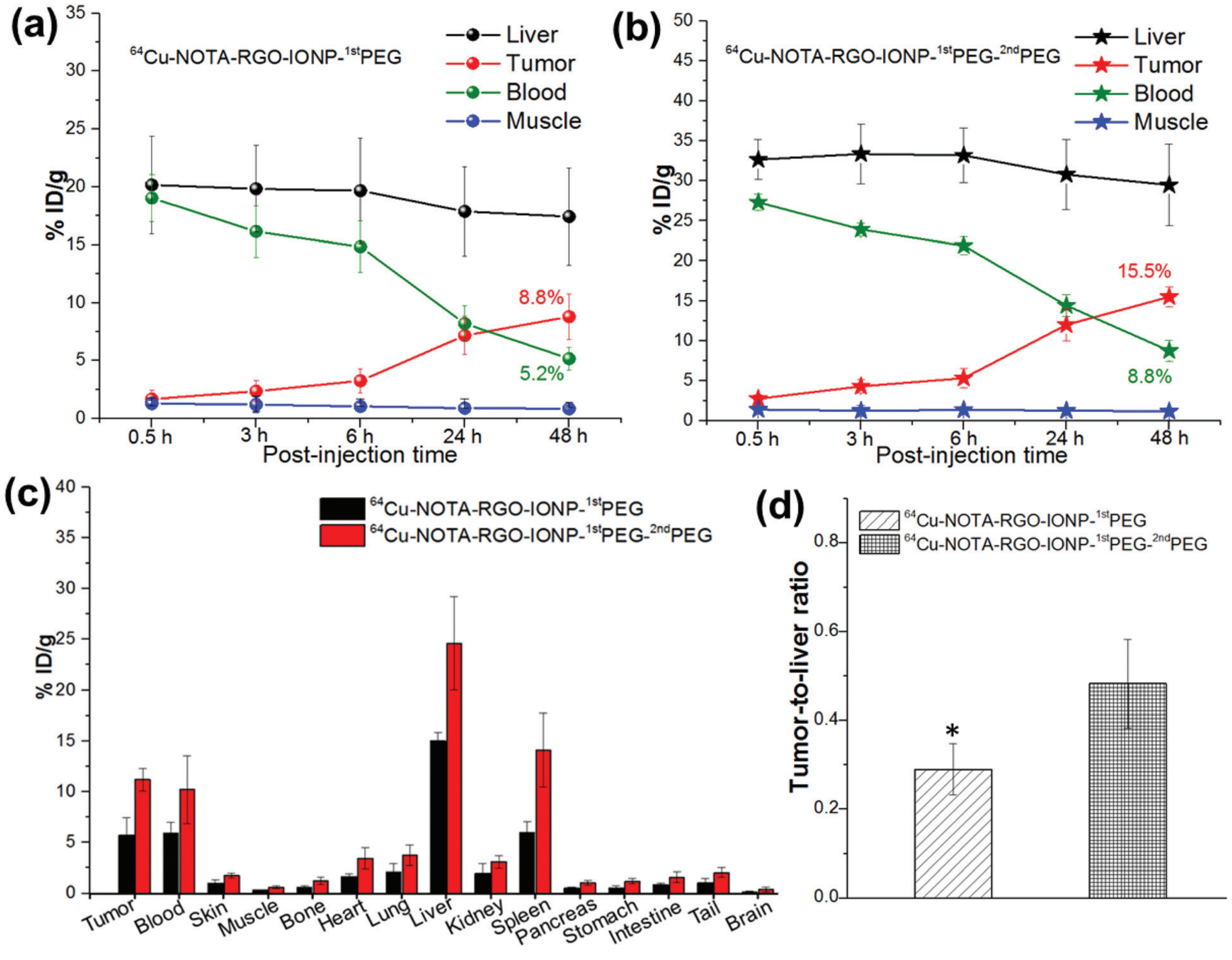

Fig. 5 Quantitative region-of-interest (ROI) analysis of the PET data. (a) Time-radioactivity uptake curves of liver, 4T1 tumor, blood and muscle after intravenous injection of ^{64}Cu-NOTA–RGO–IONP–^{1st}PEG. (b) Time–radioactivity uptake curves of liver, 4T1 tumor, blood and muscle after intravenous injection of ^{64}Cu-NOTA–RGO–IONP–^{1st}PEG–^{2nd}PEG. (c) Biodistribution studies in 4T1 tumor bearing mice at 44 h post-injection of ^{64}Cu-NOTA–RGO–IONP–^{1st}PEG (black) and ^{64}Cu-NOTA–RGO–IONP–^{1st}PEG–^{2nd}PEG (red). (d) Tumor-to-liver ratio of ^{64}Cu-NOTA–RGO–IONP–^{1st}PEG (left) and ^{64}Cu-NOTA–RGO–IONP–^{1st}PEG–^{2nd}PEG (right) based on a biodistribution study. The difference between two groups was significant (p value <0.05). All data represent 6 mice per group.

experiments (Fig. 3a and b). It should be noted that the possibly remaining ^{1st}PEG in the samples would affect the accuracy of PET imaging, since NOTA was conjugated on ^{1st}PEG.[41] To eliminate this concern, several purification methods were performed during the synthesis procedures.

The biodistribution studies of ^{64}Cu-NOTA–RGO–IONP–^{1st}PEG and ^{64}Cu-NOTA–RGO–IONP–^{1st}PEG–^{2nd}PEG were carried out at 48 h p.i. to validate the PET results (Fig. 5c). The biodistribution study and quantitative ROI analysis of PET data matched well. Even at 48 h p.i., the blood concentration of ^{64}Cu-NOTA–RGO–IONP–^{1st}PEG–^{2nd}PEG (10.2 %ID g^{-1}) was greatly higher than that of ^{64}Cu-NOTA–RGO–IONP–^{1st}PEG (5.9 %ID g^{-1}), due to the longer blood circulation. The tumor, liver and spleen uptake of ^{64}Cu-RGO–IONP–^{1st}PEG–^{2nd}PEG was 11.2, 24.6 and 14.1 %ID g^{-1} respectively. For non-renal clearable nanoparticles, the ratio of tumor-to-liver can be defined as tumor targeting specificity.[13] The tumor-to-liver ratio of ^{64}Cu-NOTA–RGO–IONP–^{1st}PEG–^{2nd}PEG (0.48) was significantly enhanced compared with ^{64}Cu-NOTA–RGO–IONP–^{1st}PEG (0.29; p-value <0.05), highlighting the superb passive tumor targeting efficiency of ^{64}Cu-NOTA–RGO–IONP–^{1st}PEG–^{2nd}PEG (Fig. 5d).

3.4 MR imaging and photoacoustic imaging

PET imaging provides high sensitivity and the quantitative tracking of radiotracers, but lacks a resolving morphology.[42] MRI with a high spatial resolution and PA imaging with deep tissue penetration were excellent complementary imaging techniques for PET. Therefore, NOTA–RGO–IONP–^{1st}PEG–^{2nd}PEG that combines the excellent magnetic property from IONPs and superb photoacoustic capacity from RGO nanosheets could serve as a promising contrast agent for both MRI (Fig. 6a–d) and PA imaging (Fig. 7a–f).

In vivo T_2-mapped MR imaging of 4T1 tumor-bearing mice was conducted before and after intravenous injection of the NOTA–RGO–IONP–^{1st}PEG–^{2nd}PEG solution with a dose of 5.8 mg Fe per kg. A darkening effect with shorter T_2 was observed in the tumor of mice at 3 h post-injection of NOTA–RGO–IONP–^{1st}PEG–^{2nd}PEG (T_2 = 40.62 ± 0.44 ms, Fig. 6b and d) and obviously enhanced at 24 h post-injection (T_2 = 30.83 ± 13.30 ms, Fig. 6c and d), compared with the same mice before the injection of nanoparticles (T_2 = 44.59 ± 11.07 ms, Fig. 6a and d), indicating passive accumulation of NOTA–RGO–

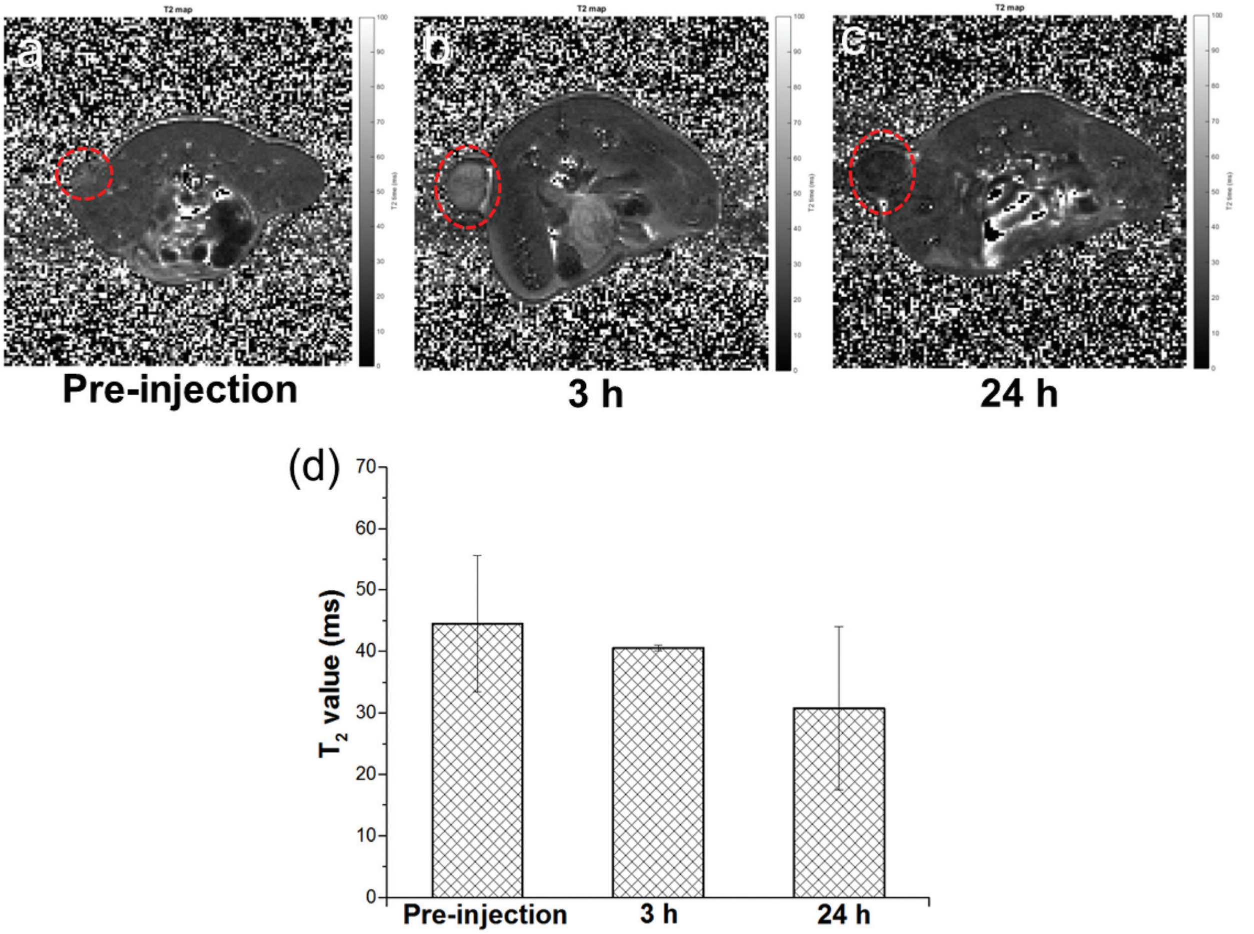

Fig. 6 *In vivo* MR imaging. *In vivo* T_2-mapped MR imaging acquired before (a) and after 3 h (b) and 24 h (c) intravenous injection of 400 μL NOTA–RGO–IONP–^{1st}PEG–^{2nd}PEG (dose: 5.8 mg Fe per kg) in the same 4T1 tumor-bearing mice (n = 2). (d) Shows the comparison of the T_2 values acquired from the tumors in the mice before and after intravenous injection of NOTA–RGO–IONP–^{1st}PEG–^{2nd}PEG.

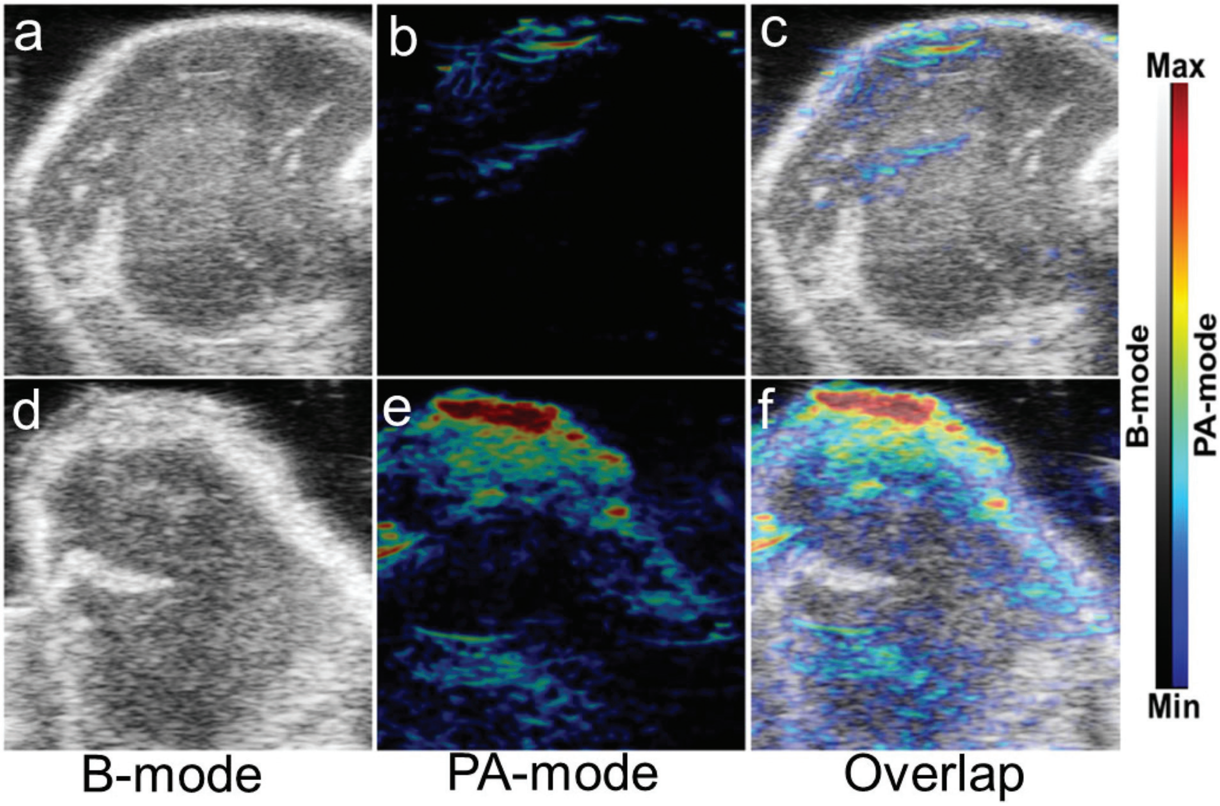

Fig. 7 *In vivo* PA imaging. (a)–(c) were the PA images of the tumor part in 4T1 tumor-bearing mouse with intravenous injection of 150 μL PBS (control group); (d)–(f) were the PA images of the tumor part in 4T1 tumor-bearing mouse with intravenous injection of 150 μL NOTA–RGO–IONP–^{1st}PEG–^{2nd}PEG (0.3 mg ml^{-1}, treated group).

IONP–^{1st}PEG–^{2nd}PEG in the tumor. Since MRI is of low sensitivity and the MR contrast highly depends on the dose of magnetic probes, a better contrast image could be achieved by increasing the concentration of injected nanoparticles.

Owing to their ability to absorb light at a wide range of wavelengths, especially in the near infra-red region, RGO-based nanomaterials are natural contrast agents for PA imaging. 4T1 tumor-bearing mice in the treated group were intravenously injected with NOTA–RGO–IONP–^{1st}PEG–^{2nd}PEG. Compared to the control group (PBS injected, Fig. 7a–c), a significantly stronger photoacoustic signal was observed from the tumor in the treated group (Fig. 7d–f). Considering that imaging and MRI display the real biodistribution of the nanoparticles, the multimodality imaging combining PA and MRI successfully confirmed that NOTA–RGO–IONP–^{1st}PEG–^{2nd}PEG indeed accumulated in the tumor site, further demonstrating the accuracy of PET imaging.

4. Conclusions

In summary, long-circulating and double-PEGylated RGO–IONP nanoparticles were developed and radiolabeled with ^{64}Cu for multimodality (PET/MR/PA) imaging with enhanced passive tumor targeting efficacy. To the best of our knowledge, a tumor accumulation of ~15.5 %ID g^{-1} was among the best achieved by inorganic nanomaterials. Our study indicates that optimization of surface PEGylation can improve the *in vivo* bioproperties of nanoparticles. Triple-modal PET/MR/PA *in vivo* tumor imaging by using RGO–IONP nanocomposites provided multi-aspect, more accurate and complete information for tumor diagnosis and therapy.

Acknowledgements

This work is supported, in part, by the University of Wisconsin–Madison, the National Institutes of Health (NIBIB/NCI 1R01CA169365, P30CA014520, T32CA009206, T32GM008505 and S10-OD018505), the American Cancer Society (125246-RSG-13-099-01-CCE), Wisconsin Distinguished Graduate Fellowship, the National Basic Research Program of China (973 Program, 2012CB932601) and the grant of China Scholarship Council. We also gratefully acknowledge the Analytical Instrumentation Center of the School of Pharmacy at University of Wisconsin–Madison for obtaining FT-IR spectra.

References

1 G. Hong, S. Diao, A. L. Antaris and H. Dai, *Chem. Rev.*, 2015, **115**, 10816–10906.

2 N. Lee, D. Yoo, D. Ling, M. H. Cho, T. Hyeon and J. Cheon, *Chem. Rev.*, 2015, **115**, 10637–10689.

3 J. V. Jokerst, T. Lobovkina, R. N. Zare and S. S. Gambhir, *Nanomedicine*, 2011, **6**, 715–728.

4 C. Xu, D. Yang, L. Mei, B. Lu, L. Chen, Q. Li, H. Zhu and T. Wang, *ACS Appl. Mater. Interfaces*, 2013, **5**, 2715–2724.

5 X. Han, Z. Li, J. Sun, C. Luo, L. Li, Y. Liu, Y. Du, S. Qiu, X. Ai, C. Wu, H. Lian and Z. He, *J. Controlled Release*, 2015, **197**, 29–40.

6 D. Pozzi, V. Colapicchioni, G. Caracciolo, S. Piovesana, A. L. Capriotti, S. Palchetti, S. De Grossi, A. Riccioli, H. Amenitsch and A. Lagana, *Nanoscale*, 2014, **6**, 2782–2792.

7 S. Shi, Y. Huang, X. Chen, J. Weng and N. Zheng, *ACS Appl. Mater. Interfaces*, 2015, **7**, 14369–14375.

8 Z. Liu, W. Cai, L. He, N. Nakayama, K. Chen, X. Sun, X. Chen and H. Dai, *Nat. Nanotechnol.*, 2007, **2**, 47–52.

9 G. Prencipe, S. M. Tabakman, K. Welsher, Z. Liu, A. P. Goodwin, L. Zhang, J. Henry and H. Dai, *J. Am. Chem. Soc.*, 2009, **131**, 4783–4787.

10 S. Shi, F. Chen, E. B. Ehlerding and W. Cai, *Bioconjugate Chem.*, 2014, **25**, 1609–1619.

11 T. Liu, S. Shi, C. Liang, S. Shen, L. Cheng, C. Wang, X. Song, S. Goel, T. E. Barnhart, W. Cai and Z. Liu, *ACS Nano*, 2015, **9**, 950–960.

12 K. Knop, R. Hoogenboom, D. Fischer and U. S. Schubert, *Angew. Chem., Int. Ed.*, 2010, **49**, 6288–6308.

13 M. Yu and J. Zheng, *ACS Nano*, 2015, **9**, 6655–6674.

14 H. Maeda, J. Wu, T. Sawa, Y. Matsumura and K. Hori, *J. Controlled Release*, 2000, **65**, 271–284.

15 X. Liu, H. Tao, K. Yang, S. Zhang, S. T. Lee and Z. Liu, *Biomaterials*, 2011, **32**, 144–151.

16 F. Chen and W. Cai, *Small*, 2014, **10**, 1887–1893.

17 Z. Sheng, L. Song, J. Zheng, D. Hu, M. He, M. Zheng, G. Gao, P. Gong, P. Zhang, Y. Ma and L. Cai, *Biomaterials*, 2013, **34**, 5236–5243.

18 C. Xu, D. Yang, L. Mei, Q. Li, H. Zhu and T. Wang, *ACS Appl. Mater. Interfaces*, 2013, **5**, 12911–12920.

19 L. Chen, X. Zhong, X. Yi, M. Huang, P. Ning, T. Liu, C. Ge, Z. Chai, Z. Liu and K. Yang, *Biomaterials*, 2015, **66**, 21–28.

20 W. Zhang, Z. Guo, D. Huang, Z. Liu, X. Guo and H. Zhong, *Biomaterials*, 2011, **32**, 8555–8561.

21 L. Feng, S. Zhang and Z. Liu, *Nanoscale*, 2011, **3**, 1252–1257.

22 K. Yang, L. Feng, H. Hong, W. Cai and Z. Liu, *Nat. Protoc.*, 2013, **8**, 2392–2403.

23 H. Hong, K. Yang, Y. Zhang, J. W. Engle, L. Feng, Y. Yang, T. R. Nayak, S. Goel, J. Bean, C. P. Theuer, T. E. Barnhart, Z. Liu and W. Cai, *ACS Nano*, 2012, **6**, 2361–2370.

24 S. Shi, K. Yang, H. Hong, F. Chen, H. F. Valdovinos, S. Goel, T. E. Barnhart, Z. Liu and W. Cai, *Biomaterials*, 2015, **39**, 39–46.

25 S. Shi, K. Yang, H. Hong, H. F. Valdovinos, T. R. Nayak, Y. Zhang, C. P. Theuer, T. E. Barnhart, Z. Liu and W. Cai, *Biomaterials*, 2013, **34**, 3002–3009.

26 S. Lee, S. W. Kang, J. H. Ryu, J. H. Na, D. E. Lee, S. J. Han, C. M. Kang, Y. S. Choe, K. C. Lee, J. F. Leary, K. Choi, K. H. Lee and K. Kim, *Bioconjugate Chem.*, 2014, **25**, 601–610.

27 J. V. Jokerst, A. J. Cole, D. Van de Sompel and S. S. Gambhir, *ACS Nano*, 2012, **6**, 10366–10377.

28 F. Chen, P. A. Ellison, C. M. Lewis, H. Hong, Y. Zhang, S. Shi, R. Hernandez, M. E. Meyerand, T. E. Barnhart and W. Cai, *Angew. Chem., Int. Ed.*, 2013, **52**, 13319–13323.

29 A. de la Zerda, J. W. Kim, E. I. Galanzha, S. S. Gambhir and V. P. Zharov, *Contrast Media Mol. Imaging*, 2011, **6**, 346–369.

30 K. Yang, L. Hu, X. Ma, S. Ye, L. Cheng, X. Shi, C. Li, Y. Li and Z. Liu, *Adv. Mater.*, 2012, **24**, 1868–1872.

31 J. Rieffel, U. Chitgupi and J. F. Lovell, *Small*, 2015, **11**, 4445–4461.

32 B. R. Jarrett, B. Gustafsson, D. L. Kukis and A. Y. Louie, *Bioconjugate Chem.*, 2008, **19**, 1496–1504.

33 J. Rieffel, F. Chen, J. Kim, G. Chen, W. Shao, S. Shao, U. Chitgupi, R. Hernandez, S. A. Graves, R. J. Nickles, P. N. Prasad, C. Kim, W. Cai and J. F. Lovell, *Adv. Mater.*, 2015, **27**, 1785–1790.

34 R. Chakravarty, H. F. Valdovinos, F. Chen, C. M. Lewis, P. A. Ellison, H. Luo, M. E. Meyerand, R. J. Nickles and W. Cai, *Adv. Mater.*, 2014, **26**, 5119–5123.

35 H. Xu, L. Cheng, C. Wang, X. Ma, Y. Li and Z. Liu, *Biomaterials*, 2011, **32**, 9364–9373.

36 Q. Fan, K. Cheng, X. Hu, X. Ma, R. Zhang, M. Yang, X. Lu, L. Xing, W. Huang, S. S. Gambhir and Z. Cheng, *J. Am. Chem. Soc.*, 2014, **136**, 15185–15194.

37 H. Sun, L. Cao and L. Lu, *Nano Res.*, 2011, **4**, 550–562.

38 C. Wang, L. Cheng and Z. Liu, *Biomaterials*, 2011, **32**, 1110–1120.

39 J. C. Harper, R. Polsky, D. R. Wheeler and S. M. Brozik, *Langmuir*, 2008, **24**, 2206–2211.

40 S. D. Li and L. Huang, *Mol. Pharm.*, 2008, **5**, 496–504.

41 H. Gong, Z. Dong, Y. Liu, S. Yin, L. Cheng, W. Xi, J. Xiang, K. Liu, Y. Li and Z. Liu, *Adv. Funct. Mater.*, 2014, **24**, 6492–6502.

42 M. S. Judenhofer, H. F. Wehrl, D. F. Newport, C. Catana, S. B. Siegel, M. Becker, A. Thielscher, M. Kneilling, M. P. Lichy, M. Eichner, K. Klingel, G. Reischl, S. Widmaier, M. Rocken, R. E. Nutt, H. J. Machulla, K. Uludag, S. R. Cherry, C. D. Claussen and B. J. Pichler, *Nat. Med.*, 2008, **14**, 459–465.